

## Analogue modelling of volcano flank terrace formation on Mars

PAUL K. BYRNE<sup>1,2\*</sup>, EOGHAN P. HOLOHAN<sup>3</sup>, MATTHIEU KERVYN<sup>4</sup>,  
BENJAMIN VAN WYK DE VRIES<sup>5</sup> & VALENTIN R. TROLL<sup>6</sup>

<sup>1</sup>*Lunar and Planetary Institute, Universities Space Research Association,  
Houston, TX 77058, USA*

<sup>2</sup>*Department of Terrestrial Magnetism, Carnegie Institution of Washington,  
Washington, DC 20015, USA*

<sup>3</sup>*German Research Center for Geosciences (GFZ Potsdam), Section 2.1: Physics of  
Earthquakes and Volcanoes, Telegrafenberg, Potsdam 14473, Germany*

<sup>4</sup>*Department of Geography, Vrije Universiteit Brussel, B-1050 Brussels, Belgium*

<sup>5</sup>*Laboratoire Magmas et Volcans, Blaise Pascal Université, 63038 Clermont-Ferrand, France*

<sup>6</sup>*Department of Earth Sciences, CEMPEG, Uppsala University, 752 36 Uppsala, Sweden*

\*Corresponding author (e-mail: [byrne@lpi.usra.edu](mailto:byrne@lpi.usra.edu))

**Abstract:** Of the features that characterize large shield volcanoes on Mars, flank terraces remain the most enigmatic. Several competing mechanisms have been proposed for these laterally expansive, topographically subtle landforms. Here we test the hypothesis that horizontal contraction of a volcano in response to the down-flexing of its underlying basement leads to flank terracing. We performed a series of analogue models consisting of a conical sand–plaster load emplaced on a basement comprising a layer of brittle sand–plaster atop a reservoir of viscoelastic silicone. Our experiments consistently produced a suite of structures that included a zone of concentric extension distal to the conical load, a flexural trough adjacent to the load base and convexities (terraces) on the cone’s flanks. The effects of variations in the thickness of the brittle basal layer, as well as in the volume, slope and planform eccentricity of the cone, were also investigated. For a given cone geometry, we find that terrace formation is enhanced as the brittle basement thickness decreases, but that a sufficiently thick brittle layer can enhance the basement’s resistance to loading such that terracing of the cone is reduced or even inhibited altogether. For a given brittle basement thickness, terracing is reduced with decreasing cone slope and/or volume. Our experimental results compare well morphologically to observations of terraced edifices on Mars, and so provide a framework with which to understand the developmental history of large shield volcanoes on the Red Planet.

The most distinctive of Mars’ volcanic attributes is arguably its population of enormous shield volcanoes – the largest of which, Olympus Mons, stands some 22 km above its surrounding plains (Plescia 2004). These shields host a range of recognized volcanic features, including summit caldera complexes, abundant lava flows, parasitic shields and pit craters (e.g. Crumpler & Aubele 1978; Mouginiis-Mark *et al.* 1984; Zimbleman & Edgett 1992; Hodges & Moore 1994; Plescia 2000; Wyrick *et al.* 2004; Bleacher *et al.* 2007; Byrne *et al.* 2012). Interestingly, of the 22 largest Martian shields, a subset also possesses laterally expansive, topographically subtle undulations on their slopes, termed ‘flank terraces’.

Terraces were first observed on the upper flanks of Olympus Mons (Carr *et al.* 1977; Morris 1981),

and were later reported on the flanks of the three Tharsis Montes, Arsia, Pavonis and Ascraeus (Thomas *et al.* 1990). Their low relief and broad planform render flank terraces difficult to see with conventional photogeological data, however, and so a detailed assessment of their morphology and distribution (both on a given volcano and across Mars) was not possible until the availability of the near-global Mars Orbiter Laser Altimeter (MOLA) digital elevation model (DEM) dataset (Smith *et al.* 2001).

Using MOLA-derived slope maps, Byrne *et al.* (2009) identified terraces on the flanks of at least nine Martian shields – Alba, Arsia, Ascraeus, Elysium, Olympus, Pavonis and Uranus Montes, and Albor and Hecates Tholi – arranged systematically in a partially or fully axisymmetrical imbricate

'fishscale' pattern about each volcano (Fig. 1). Terraces are convex-outwards, convex-upwards landforms with a near-flat upper surface, the slope of which increases towards the terrace base. Scale-invariant features, terraces are expressed across a range of geometrical sizes: the average terrace length for each of these nine volcanoes spans 12–51 km, and the vertical relief ranges from 0.1 to 1.3 km (Byrne *et al.* 2009).

Their morphological similarity to the lobate surface traces of thrust faults motivated early workers to interpret flank terraces as shortening structures. In their study of Olympus Mons, Thomas *et al.* (1990) concluded that compression of the volcano as a result of self-loading led to terrace formation via thrust faulting. McGovern & Solomon (1993) also argued for thrust-fault-related terracing, but concluded that this deformation resulted from compression of a volcano as its weight caused sagging, or down-flexing, of the underlying lithosphere (e.g. Zucca *et al.* 1982). Alternatively, Crumpler *et al.* (1996) suggested that inflation of a magma chamber situated high in a volcano could steepen its upper flanks through uplift of material along inwards-dipping reverse faults and so produce terraces. Later, Morgan & McGovern (2005) and McGovern & Morgan (2009) suggested that the terraces on Olympus Mons are due to a combination of thrust faulting and slumping as the edifice spread. Following analysis of flank terrace morphology and distribution across nine volcanoes on Mars, Byrne *et al.* (2009) found no convincing evidence for self-loading, magma chamber tumescence or volcano spreading as terrace formation mechanisms, but considered volcano-induced lithospheric flexure (i.e. volcano sagging) to be a plausible candidate process.

To further test the hypothesis of an origin for flank terracing through lithospheric flexure requires a modelling approach. Past studies have mainly used numerical models (e.g. McGovern & Solomon 1993), but these have been continuum-based and so did not directly reproduce the discontinuous structures that terraces might represent. Analogue models surmount this difficulty and so allow for the formation of such structures, such that their spatial and temporal development can be characterized. Williams & Zuber (1995) incrementally emplaced a conical load upon a basement composed of an agar–sand–gelatine plate overlying a substrate of corn syrup. This produced a flexural trough and annular fissures around the conical load, but the material used for the load (lead gunshot) was too coarse to reveal the structural effect of flexure upon the load itself. In contrast, Kervyn *et al.* (2010) and Byrne *et al.* (2013) emplaced conical sand–plaster loads upon a basement of the same material, overlying a silicone

polymer substrate. This model set-up produced convex-outwards, convex-upwards structures on the conical load's flanks.

The purpose of this chapter is to complement those of Kervyn *et al.* (2010) and Byrne *et al.* (2013) by reporting more detailed experimental observations of flank terrace formation in analogue models of a volcano down-flexing its lithospheric basement. In particular, we report new observations of the kinematics of terrace development, and on how model terracing is affected by changes in the geometry of the basement and the cone. We also compare the model structures in detail to those observed on Mars. Our results provide an improved basis for understanding gravitational deformation of large shield volcanoes on Mars in particular, and on terrestrial planets in general.

## Experimental methods

In this study, we simulated volcano-induced flexure by emplacing a brittle sand–plaster cone atop a basement consisting of brittle upper and ductile lower substrata (Fig. 2). The cone and basement serve as analogues to a Martian shield and its underlying lithosphere, respectively. The system deformed in response to the load of the cone. Several parameters in the experimental set-up, including the thickness of the brittle upper layer, as well as the volume, slope and plan-view aspect ratio of the cone, were then varied.

### Analogue materials

Fine (*c.* 300  $\mu\text{m}$  mean grain diameter) aeolian quartzose sand served as a granular analogue to rocks of the Martian volcanic edifices and of the planet's upper lithosphere. Dry sand is a suitable analogue for such rocks as it undergoes plastic deformation that, at model normal stresses, is characterized by brittle failure in approximate accordance with a Navier–Coulomb failure criterion (Hubbert 1951; Merle & Borgia 1996; Schellart 2000; Lohrmann *et al.* 2003). When mixed in a 10:1 ratio with powdered gypsum to increase its cohesion, the material had a bulk density of approximately  $1400 \text{ kg m}^{-3}$ , an angle of repose of  $33^\circ$  and cohesion of 50–100 Pa (Donnadieu & Merle 1998; Walter & Troll 2001; Cecchi *et al.* 2005; Delcamp *et al.* 2008).

A transparent silicone putty (polydimethylsiloxane (PMDS), commercially produced by Dow Corning® as Silastic SGM 36; ten Grotenhuis *et al.* 2002) simulated the rocks of the lower, viscoelastic lithosphere. At low experimental strain rates, silicone putty is an effective analogue to material with a rheology that is ductile over geological

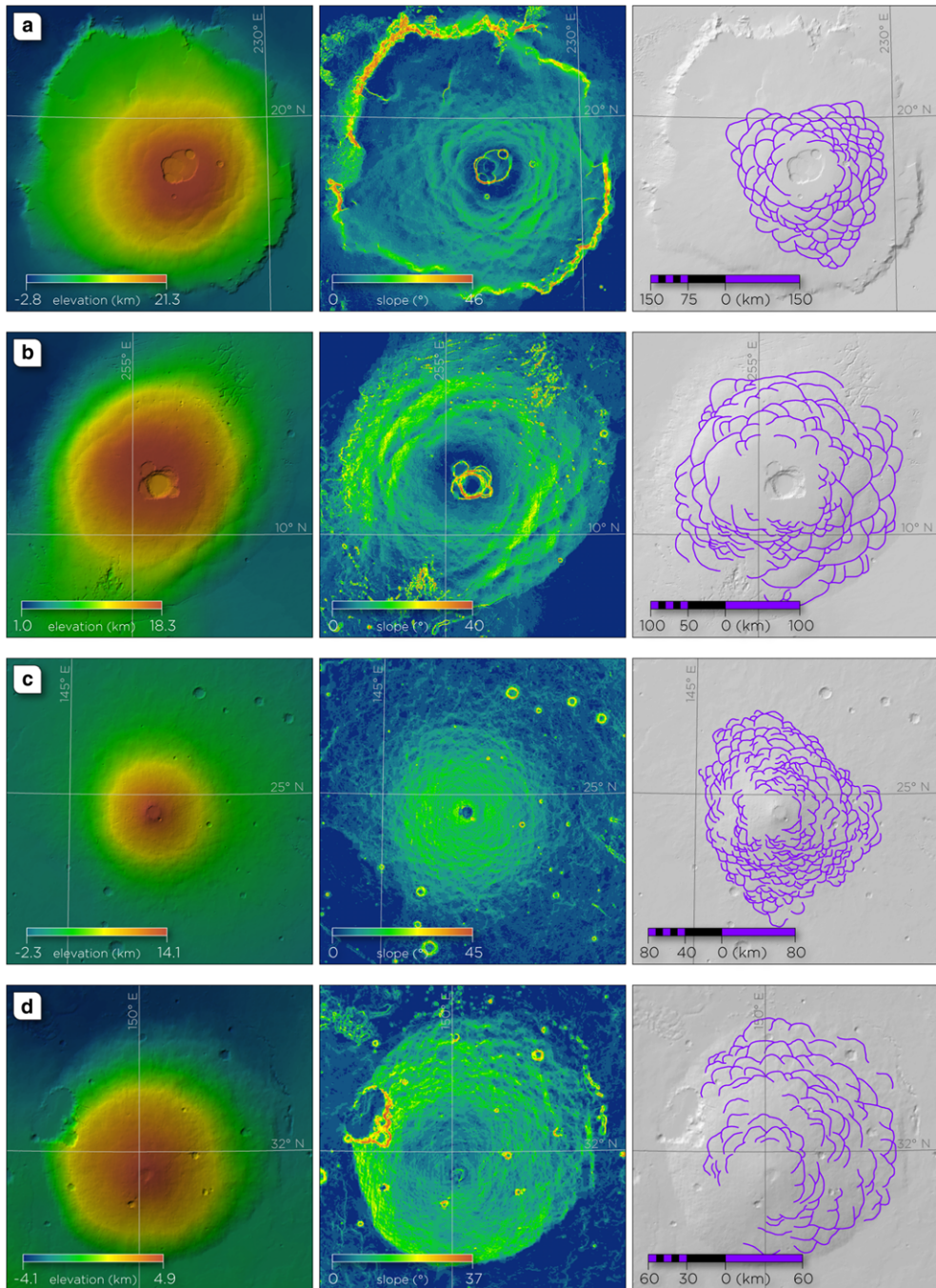


**Fig. 1.** Four exemplar Martian shield volcanoes that display flank terraces, shown in composite colour-coded elevation and hillshade maps (left column), in slope maps (centre column) and as hillshade maps with terrace outlines in purple (right column). (a) Olympus Mons, (b) Ascraeus Mons, (c) Elysium Mons and (d) Hecates Tholus. Elevation, slope and hillshade data are from the 128 pixel-per-degree MOLA dataset (Smith *et al.* 2001). Terrace maps are from Byrne *et al.* (2009). Hillshade maps are shown with illumination from the NW and at a declination of 45°. Each map is shown in an azimuthal equidistant projection, centred at (a) 18.5°N, 226°E, (b) 11.5°N, 255.5°E, (c) 25°N, 147°E and (d) 32°N, 150°E.

timescales (e.g. Weijermars *et al.* 1993; Merle & Borgia 1996; ten Grotenhuis *et al.* 2002; Oehler *et al.* 2005). Mixed with about 1% by weight of quartzose sand, the putty had a bulk density of approximately  $1200 \text{ kg m}^{-3}$  and a viscosity of

$4 \times 10^4 \text{ Pa s}$  at experimental conditions (Delcamp *et al.* 2008; Byrne *et al.* 2013).

### Standard experimental procedure

The experimental apparatus consisted of a 1 m-high, 48 cm-diameter cylindrical container, into which an 80 cm-thick silicone layer was placed first, followed by the addition, via sieving, of a 30 mm-thick sand–plaster substratum (Fig. 2a) (Table 1). Sand–plaster mix of sufficient volume to form a cone 25 cm in diameter ( $c. 1325 \text{ cm}^3$ ) was then poured directly upon the sand–plaster layer, its angle of repose resulting in flank slopes of around  $33^\circ$  and a height of approximately 8 cm (see the ‘Model scaling’ subsection below). The cone was smoothed by sieving more sand onto its flanks, before a thin ( $< 1 \text{ mm}$ ) layer of plaster was sieved over the entire model to preserve any small-scale structures that might form.

The basement responded to the cone’s weight almost immediately, sometimes resulting in a flexural depression even before delivery of the cone was complete. Consequently, the time for cone emplacement was restricted to less than 60 s. Cone emplacement was therefore effectively instantaneous, corresponding to only the very fastest effusion rates theorized for Mars (e.g. Isherwood *et al.* 2013) and to numerical models with instantaneous loads (e.g. McGovern & Solomon 1993).

All experiments were incrementally photographed in high spatial resolution from plan view. High-incidence-angle illumination (relative to the surface normal) was used, to highlight any subtle deformation. In most cases, structures had formed within 600 s of cone emplacement, with very little new surface strain apparent after 1200 s. Silicon carbide (SiC) particles, the dark colour of which strongly contrasted with the lighter sand–plaster mix, were added to the cone surfaces to help focus the overhead camera.

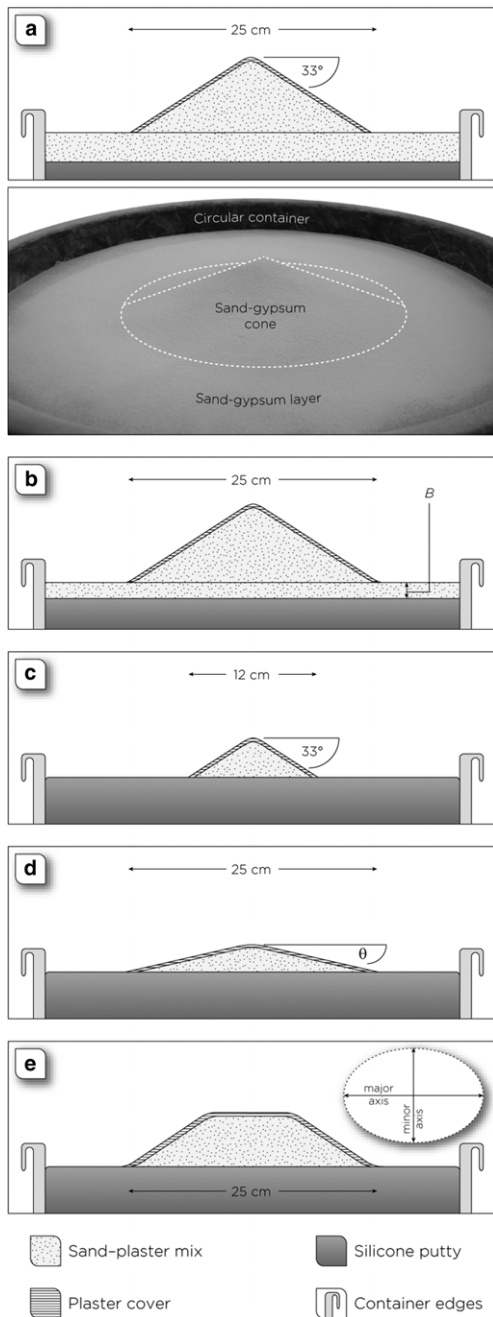


**Fig. 2.** (a) Schematic cross-section (top) and photograph (second from top) of the standard experimental set-up. The cross-section shows the sand–plaster cone, plaster cover, brittle upper-basal layer, silicone putty and the edges of the container in which the model was constructed. The photograph shows the inner wall of the container, the surface of the brittle upper layer and the model cone itself (its outline is dashed in white). Below the photograph, schematic cross-sections are shown for experiments where (b) brittle-layer thickness ( $B$ ), (c) cone volume, (d) cone slope ( $\theta$ ) and (e) cone eccentricity (with major and minor axes labelled on a schematic of the cone’s planform) were varied. The cone in (e) is drawn along its major axis; its slopes are at the angle of repose. Sketches show only the upper part of the (typically 80 cm-deep) experimental set-up.

**Table 1.** List of model parameters in experiments of (a) standard volcano loading, as well as models in which (b) basal brittle-layer thickness,  $B$ , (c) cone volume, (d) cone slope,  $\theta$  or (e) cone aspect ratio was varied\*

Experiment	Cone diameter (cm)	Cone slope ( $^{\circ}$ )	Cone volume ( $\text{cm}^3$ )	Cone height (cm)	Brittle-layer thickness (mm)	Number of experiments
(a) Volcano loading	25	33	1325	8.1	<b>30</b>	5
	25	33	1325	8.1	<b>70</b>	1
	25	33	1325	8.1	<b>20</b>	1
(b) Variation in basal sand–plaster layer thickness, $B$	25	33	1325	8.1	<b>15</b>	1
	25	33	1325	8.1	<b>10</b>	1
	25	33	1325	8.1	<b>5</b>	2
	25	33	1325	8.1	<b>2</b>	1
	25	33	1325	8.1	<b>0</b>	4
(c) Variation in cone volume	12	33	<b>147</b>	3.9	0	4
	25	<b>5</b>	1325	1.1	0	1
	25	<b>10</b>	1325	2.2	0	1
(d) Variation in cone slope, $\theta$	25	<b>20</b>	1325	4.5	0	2
	25	<b>25</b>	1325	6.4	0	1
	25	<b>30</b>	1325	7.2	0	1
	<b>25/17</b>	33	<b>1770</b>	8.1	0	3

\*Changes in a model parameter from that described as part of the standard experimental set-up are shown in bold. The total number of experiments performed in this study is 29.

To quantify horizontal displacements and strain fields in the models, particle image velocimetry (PIV) analyses of the experiment photographs were performed by using LaVision DaVis 7.2 digital image correlation software (cf. Walter 2011). The PIV results are displayed as incremental horizontal displacement fields, together with dilational strain derived from the components of the two-dimensional (2D) infinitesimal displacement gradient tensor (Holohan *et al.* 2013). Here, we generally interpret dilation, a measure of the increase or decrease in horizontal surface area, in terms of overall horizontal extension and contraction, respectively.

### Variations in experimental parameters

Key experimental parameters were varied to assess the effects of flexure under a range of geometrical scenarios representative of those observed or inferred for Martian shields (Table 1). First, we chose to model variations in thickness of the brittle upper Martian lithosphere,  $B$ . For the oceanic lithosphere on Earth, which is thought to be chemically and structurally similar to the Martian lithosphere, the seismogenic (i.e. brittle) thickness is commonly similar to estimates of effective elastic thickness,  $T_e$  (cf. Watts & Burov 2003). A range of  $T_e$  values for Mars has been calculated by examining crustal deformation related to large surface loads (e.g. Comer *et al.* 1985) or by modelling gravity/topography admittances from gravity

and topographical data (e.g. Zuber *et al.* 2000; McGovern *et al.* 2004; Belleguic *et al.* 2005). Given then the calculated differences in  $T_e$  beneath large Martian shields (e.g. table 3 in McGovern *et al.* 2004) and the expected commensurate effect upon flexural response, we performed a series of experiments in which  $B$  was varied from 70 to 2 mm by uniformly sieving sand–plaster layers of different thicknesses directly upon the silicone prior to cone emplacement (Fig. 2b, Table 1), as well as a number of experiments where  $B = 0$  (i.e. the brittle upper layer was absent altogether).

Edifice volume on Mars varies by almost four orders of magnitude (Plescia 2004), and so several experiments were conducted with a poured cone volume (*c.*  $147 \text{ cm}^3$ ) that was approximately 11% of that in the standard set-up. These lower-volume cones had a basal diameter of 12 cm (Fig. 2c), a height of approximately 4 cm and a slope of around  $33^{\circ}$  (see the subsection on ‘Model scaling’ below). To account for an order-of-magnitude variation in Martian flank slopes (Plescia 2004), we also varied model cone slopes ( $\theta$ ) from  $30^{\circ}$  to  $5^{\circ}$  in increments of  $5^{\circ}$  (Fig. 2d). These cones were constructed by sieving rather than by pouring. Finally, volcanic loads with non-axisymmetrical planforms were simulated. Whilst some Martian shields appear relatively circular in plan view (e.g. Elysium Mons: Plescia 2004), others have a pronounced ellipticity. An example is Ascraeus Mons, the construction of which has been influenced by a SW–NE regional structural trend (Byrne *et al.*

2012) (contrast Fig. 1b, c). We therefore additionally modelled cones with an eccentricity of 1:1.5 (short:long axes in plan view) (Fig. 2e). These latter experimental parameters (edifice volume, slope and planform) were investigated by using a model set-up in which  $B = 0$ . This experimental configuration was motivated by the observation that the suite of structures formed during flexure was essentially unchanged compared with models that featured higher, more realistic values of  $B$ .

### Model scaling

Material properties and forces in analogue experiments should geometrically, kinematically and dynamically scale to nature (Hubbert 1951; Ramberg 1981) (Table 2). The scaling ratio for any physical property is defined as:

$$X^* = X_{\text{model}} \times (X_{\text{nature}})^{-1} \quad (1)$$

The length ratio ( $l^* = l_{\text{model}} \times (l_{\text{nature}})^{-1}$ ) is the geometric scaling factor for these experiments and is  $10^{-6}$ , such that 1 cm in the models represented 10 km in nature. A model radius of 12.5 cm therefore corresponded to a volcano 250 km in diameter, whilst a cone radius of 6 cm scaled to a volcano diameter of 120 km, representative, respectively, of a medium-sized (e.g. Uranus Patera) and small (e.g. Tharsis Tholus) shield volcano on Mars (Plescia 2004).

However, this length ratio scaled our approximately 8 and 4 cm-high model cones (Table 1) to natural cones of around 80 and 40 km in height, values that are in excess of the true natural range (Plescia 2004) (even accounting for underestimation due to infilling of flexural troughs: e.g. Zucca *et al.* 1982; Byrne *et al.* 2013). Nevertheless, experiments with model slopes comparable to Martian volcanoes (i.e.  $5^\circ$ ) and heights of about 1 cm (corresponding to a volcano 10 km tall) displayed similar surface deformation patterns to cones at the angle of repose (see the subsection on ‘Experimental parameter variations’ below). This comparable

behaviour, together with similarities to the predictions of terracing in numerical studies that considered a very low-slope edifice geometry (e.g. McGovern & Solomon 1993; Borgia 1994; Van Wyk de Vries & Matela 1998), lead us to conclude that even with unrealistic scaled model heights, the overall structural resemblance between our analogue model results and natural volcanoes with low slopes are meaningful. Further, we note that although cone height in angle-of-repose models is not geometrically similar to nature, models with very low flank slopes (e.g.  $5\text{--}10^\circ$ ) accurately scale to Martian shields approximately 20–10 km in relief (Plescia 2004).

A model upper-lithosphere brittle-layer thickness of 2–70 mm (Table 1) correlates to natural values of 2–70 km. This variation in  $B$  is comparable to the range of gravity/topography admittance-derived  $T_e$  estimates for Arsia Mons (McGovern *et al.* 2004; Belleguic *et al.* 2005), and is similar to those values for Ascraeus and Pavonis Montes, and for the Elysium Rise as a whole (McGovern *et al.* 2004). Our range in  $B$  values is also broadly in line with those calculated by Beuthe *et al.* (2012) using top- and bottom-loading models of the Martian lithosphere.

The dynamic scaling factor is the scale ratio for stress and cohesion, and is given by the relationship:

$$\sigma^* = l^* \times g^* \times \rho^* \quad (2)$$

where  $l^*$  is the length ratio,  $g^*$  is the ratio of accelerations due to gravity and  $\rho^*$  is the density ratio. At sea level on Earth,  $g$  is  $9.81 \text{ m s}^{-2}$ , whilst equatorial surface gravity on Mars is  $3.71 \text{ m s}^{-2}$ ;  $g^*$  is thus 2.64. The density of the sand–plaster mix used in these experiments is approximately  $1400 \text{ kg m}^{-3}$ , whereas Martian crustal density is assumed to be about  $2600 \text{ kg m}^{-3}$ , such that  $\rho^*$  is  $5.38 \times 10^{-1}$ . The stress ratio, from equation (2), is therefore  $1.42 \times 10^{-6}$ . From this, a rock cohesion on Mars of  $5 \times 10^7 \text{ Pa}$  should scale to a model cohesion of around 70 Pa, comparable to the low-cohesion sand–plaster mix used.

**Table 2.** Scaling parameters, values for models and Mars and scaling ratios used in this study

Parameter	Symbol	Units	Model	Nature	Ratio
Length	$l$	m	$1 \times 10^{-2}$	$1 \times 10^4$	$1 \times 10^{-6}$
Gravity	$g$	$\text{m s}^{-2}$	$9.81 \times 10^0$	$3.71 \times 10^0$	$2.64 \times 10^0$
Stress	$\sigma$	Pa	$1.37 \times 10^2$	$9.65 \times 10^7$	$1.42 \times 10^{-6}$
Time	$T$	s	$2.91 \times 10^2$	$1.04 \times 10^{12}$	$2.81 \times 10^{-10}$
Density	$\rho$	$\text{kg m}^{-3}$	$1.4 \times 10^3$	$2.6 \times 10^3$	$5.38 \times 10^{-1}$
Cohesion	$C$	Pa	$7.1 \times 10^1$	$5 \times 10^7$	$1.42 \times 10^{-6}$
Viscosity	$\mu$	Pa s	$4 \times 10^4$	$1 \times 10^{20}$	$4 \times 10^{-16}$

The behaviour of Coulomb materials is theoretically independent of time, but the deformation of a ductile material is rate-dependent. A time ratio,  $T^*$ , can be calculated (Donnadieu & Merle 1998) as:

$$T^* = \mu^* \times (\sigma^*)^{-1} \quad (3)$$

where  $\mu^*$  is the viscosity ratio and  $\sigma^*$  is the stress ratio given above. The viscosity of the silicone used in the experiments is  $4 \times 10^4$  Pa, but the viscosity of the Martian ductile lithosphere is unknown. However, assuming it is composed largely of mafic lithologies (e.g. McSween *et al.* 2003), we consider a value of  $10^{20}$  Pa to be reasonable (Watts & Zhong 2000). The viscosity ratio,  $\mu^*$ , is thus  $4 \times 10^{-16}$ , giving a time ratio,  $T^*$ , of  $2.81 \times 10^{-10}$ .

We note that the ratio between the densities of the granular material and silicone putty is at the upper end, or slightly in excess, of the natural range (Belleguic *et al.* 2005), which may have enhanced the 'sink potential' (Borgia *et al.* 2000) of our models. This experimental limitation is probably minor, however, since the main effect of the greater density of the overlying brittle material would only be to increase the rate of sagging (which is itself poorly understood). An increased sagging rate should not fundamentally alter the associated brittle deformation on the volcano and in the surrounding basement.

### Volcano-induced flexure model results

Four distinct structural elements characterized all volcano load-induced flexural experiments in this study: flank convexities; a bowl-shaped depression; a load-centric trough; and an annular zone of extension (cf. Kervyn *et al.* 2010; Byrne *et al.* 2013). Here we first report spatial and temporal observations for a standard volcano-loading experiment, and then we describe the results of models in which parameters were varied with respect to those of the standard experimental set-up.

#### Volcano loading

Where an axisymmetrical cone at the angle of repose was placed directly upon a basement consisting of an upper, brittle stratum 30 mm thick and a lower, ductile stratum (Fig. 3a), the load down-flexed, and sagged rapidly into, the basement (Fig. 3b). As a consequence, the cone experienced a reduction in basal diameter and a shortening of flank length.

A set of convex-upwards, outwards-verging terraces, arranged concentrically in an imbricate stacking pattern, formed on the cone as flank shortening proceeded (Fig. 3c: 1). The leading edges of these features were manifest as ridge-like bounding

scarps. The longest terraces, laterally continuous for several tens of degrees of arc, occurred at mid-flank elevations. Vertical relief on terraces was typically of the order of 1 mm, although some examples accumulated relief of several mm along their leading edges. More subtle structures were visible with high-incidence-angle illumination, which showed them to be present on all flank sectors (i.e. at all azimuths). Flank convexities were greatest in number at mid- to lower-flank elevations; few, if any, terraces were observed near the summit.

A broad, shallow, bowl-shaped flexural depression developed in the basement as the load sank, and remained visible upon removal of the cone and the brittle layer. The flexural bowl fully enclosed the cone and was itself bounded by a very subtle topographical rise. The bowl's base was near-flat, with some diapirism of the silicone putty producing a knotted texture at its centre. The opposing slopes of the bowl, and the lower flanks of the cone, together defined a shallow flexural trough around the load (Fig. 3c: 2).

Finally, an annular pattern of arcuate and en echelon fractures developed immediately outside the flexural trough to mark a circular system of extension concentric to the load (Fig. 3c: 3). Intersecting fractures formed discrete blocks within this extensional zone, which transitioned in places to arcuate or wholly load-centric systems of half-graben or graben bounded by steep scarps. As sagging continued, the annulus tended to broaden, its inner edge moving towards the cone.

Analyses of sequential photographs of a representative standard experiment provide a useful insight into the temporal development of these flexural structures. Whilst unequivocal model terraces are visible within about 5 min of loading, it may be that some formed even sooner. The insets in Figure 3b show terraces at the base (black outline) and at mid-flank elevations (white outline) of a model cone after deformation had ceased. The leading edges of these structures are characterized by arcuate traces of shadowed sand grains (as illumination is from the top left). Corresponding insets in Figure 3a show morphologically similar, albeit much more subtle, shadowed arcuate convexities at the same positions on the cone within 60 s of its delivery.

The PIV analysis of the time-lapse images yields further insight into the development of experimental strain. Figure 3d–f shows deformation in the horizontal plane (i.e. orthogonal to the downwards-looking camera) in 120 s increments at 3, 5 and 7 min from the start of flexure. The PIV shows that the cone experiences an initial overall horizontal contraction (shown in blue), within which there are sharp gradients that clearly demarcate the analogue terrace boundaries. In contrast,

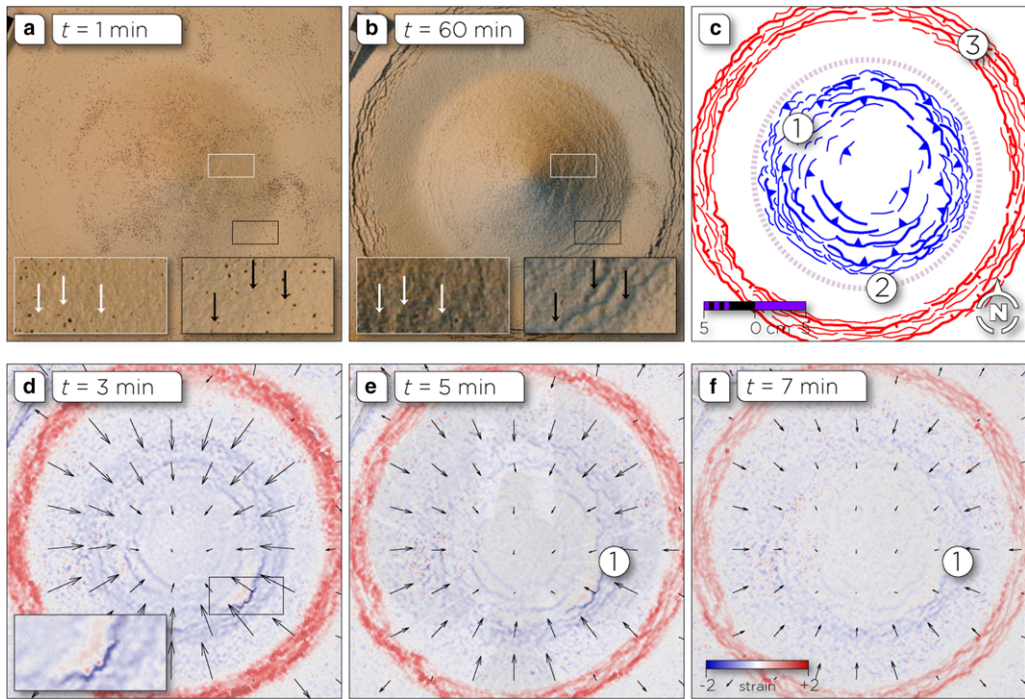


**Fig. 3.** Photographs of a representative volcano-loading experiment at (a) 1 min and (b) 60 min after the onset of sagging. The insets show subtle convexities (a) and fully formed terraces (b) on the mid (white outline) and lower (black outline) flanks of the model cone. Illumination in these images is from the NW. (c) Structural sketch of the cumulative experiment deformation in (b). (1) Terrace traces are outlined in blue (flags are on the inferred hanging wall), (2) the axis of the flexural trough is marked by a grey dashed line, whilst (3) fissures, normal faults and graben are shown in red (ticks are on the downthrown side of faults). (d)–(f) PIV images of horizontal displacements (extension denotes red, contraction denotes blue) across the same experiment 3, 5 and 7 min after flexural onset. The inset in (d) shows localized extension behind the leading edges of some model terraces. Note that the longest duration of terrace activity occurs on the lowermost flanks of the cone (e and f: 1).

a broad horizontal extension (shown in red) characterizes the distal concentric fracture system, with sharp gradients in extension closely associated with individual fissures and normal faults. The zone of central horizontal contraction arises from the inwards horizontal motion of the cone–basement system. This inwards motion peaks between the cone and the concentric fracture system, and decreases towards the cone summit. The zone of peripheral horizontal extension results from the divergence in horizontal displacement vectors associated with the formation of a surrounding flexural bulge.

As the experiment progressed, terraces on the cone’s upper and mid flanks stopped accumulating strain, whereas those at lower elevations continued to develop. The zone of active deformation therefore appeared to focus with time on the lower flanks. In some models, there was a clear downwards progression of terrace formation, somewhat like the behaviour of an ‘in-sequence’ propagating

fold-and-thrust belt. Consequently, the terraces towards the cone base stayed active for the greatest length of time. These terraces were often the largest, and commonly showed an area of extension just inside their leading edge (inset in Fig. 3d). The duration and magnitude of this extension appeared to be closely linked to that of the strain accumulation of the associated terraces (Fig. 3e: 1 and Fig. 3f: 1).

#### *Experimental parameter variations*

The inclusion of basal sand–plaster layers of thicknesses  $B < 30$  mm had a noticeable, if subtle, effect on the expression of flank convexities and extensional zones (Fig. 4). With thinner brittle layers, the spacing between terraces on the cone decreased so that more, although shorter, convexities formed, especially at mid-flank elevations (Fig. 4a: 1;  $B = 15$  mm). Smaller terraces continued to populate lower cone elevations (Fig. 4a: 2). Notably, as  $B$

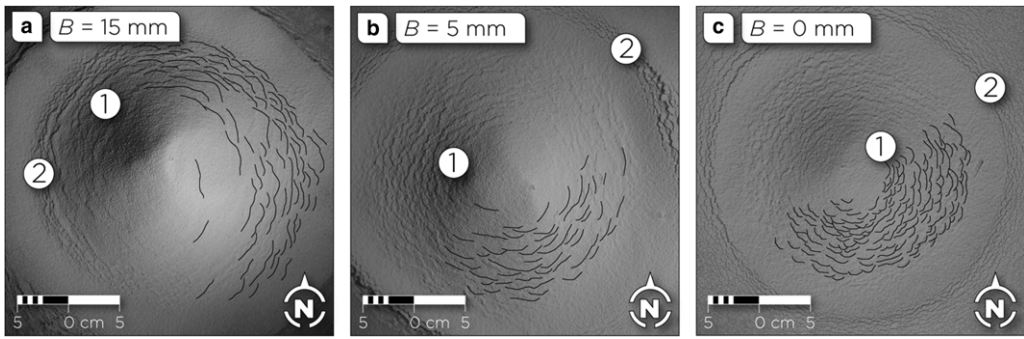


**Fig. 4.** Model cones 25 cm in diameter and at the angle of repose, but for which brittle-layer thickness,  $B$ , was (a) 15 mm, (b) 5 mm and (c) 0 mm (i.e. absent). (a: 1) Few terraces form high on the cone, but more, shorter terraces develop at mid-flank elevations; (a: 2) the lower flanks are substantially terraced. (b: 1) Terraces populate the mid to upper flanks, whilst (b: 2) the width of the annular zone of extension is reduced. (c: 1) Where the brittle layer is not present, terraces are smaller and are distributed across all flank elevations, even close to the summit, and (c: 2) the load-concentric fractures are smaller, but define a wider extensional annulus. In all images, illumination is from the SE or east; black lines are terrace traces on the experiment visible only from other illumination azimuths, and are included here for clarity.

decreased, terraces began to form progressively closer to the summit (Fig. 4b: 1;  $B = 5$  mm). This trend continued even when the brittle layer was absent entirely. Where  $B = 0$ , the greatest difference in how the suite of structures was manifest was the increased number, but decreased size, of flank convexities, which were distributed almost to the summit (Fig 4c: 1; cf. Fig. 3b).

Lower  $B$  values also resulted in deeper and narrower flexural depressions, as reflected in a decreased radial distance from the topographical bulge to the load summit. As  $B$  tended to zero, the radial width of the annular fracture zone increased (Fig. 4b: 2), although the constituent fractures

individually accumulated less strain (Fig. 4c: 2). Other differences associated with decreasing  $B$  values included a tendency for the extensional annulus to occur closer to the cone, reflecting the reduced diameter of the flexural depression, and for the inwards-facing wall of the flexural trough to transition from a state of extension to one of contraction as down-sagging ensued (visible using PIV). Conversely, increasing  $B$  inhibited basement flexure, such that, at  $B \geq 70$  mm, the related structures (including terraces) were no longer detectable.

Reduced-volume cones at the angle of repose (Fig. 5a) resulted in proportionately reduced

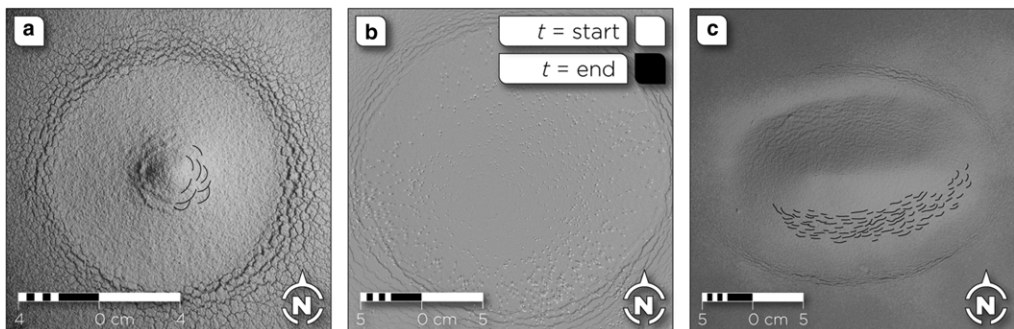


**Fig. 5.** Models with other geometric parameters varied. (a) A low-volume ( $147 \text{ cm}^3$ ) cone with slopes at the angle of repose. (b) A cone 25 cm in diameter with slopes of  $10^\circ$ , where images of the start and end of the experiment have been overlain, and the colours of the former inverted, to show the relative motion of SiC grains on the cone surface over the course of the model's deformation. The path from white to black particles gives the direction of movement of individual grains as the experiment progressed. (c) A cone with a planform eccentricity of 1:1.5 ( $25 \times 17$  cm) with slopes at the angle of repose. Illumination in (a) is from the east and in (c) the SE.

expressions of the flexural bowl, the load-concentric trough and the extensional annulus. Notably, the number of individual terraces that formed was consistently lower in these experiments. Otherwise, the characteristic suite of flexural structures developed as for models using the standard experimental set-up.

A greater difference in the expression of flank deformation was apparent in experiments where cone slopes were reduced. Compared with angle-of-repose models with the same diameter, models that featured cones with lower slopes produced shallower depressions in the silicone and showed less overall surface displacement. Flexural bowls, troughs and concentric fracture zones developed as before, but were less well expressed. Terraces were easily visible on 15–30° slopes, but were difficult to detect below this threshold (even with high-incidence-angle illumination). However, photographic sequences of model cone flanks, even to slopes of 5°, show the same gross kinematic behaviour as angle-of-repose cones. Specifically, individual sand and SiC grains inside the boundary of the annular extensional zone moved towards the centre of the load, shortening the radial and concentric distances between each other. This behaviour is shown for a cone with slopes of 15° in Figure 5b, in which photographs of the start and end of the experiment have been overlain, and the colours of the former inverted. The relative motion of SiC grains on the cone's surface is clearly visible, even in the absence of obvious flank terracing. Particles beyond the annular fractures behaved in the opposite manner, moving away from the load and from one another.

In experiments with cones of elliptical planform, the entire suite of flexural structures formed as for the standard set-up, but the distribution of flank terracing differed (Fig. 5c). Rather than forming a generally axisymmetrical pattern, the number and expression (length and vertical relief) of terraces were greatest on the sectors parallel or near-parallel to the long axes of elliptical model cones. PIV data show that the greatest horizontal strains were accommodated on these same sectors.

## Discussion of model deformation

Observations of the structural outcomes of each experimental configuration, sequential photography and PIV analyses together provide a framework from which to understand the kinematic development of our volcano-induced flexure models. We first summarize the development of structures in a representative standard volcano-loading experiment, and then review the effects of parameter variations upon model deformation.

### *Model terrace formation*

On the basis of their convex-upwards shape, outwards vergence and formation within a body undergoing net horizontal contraction, we interpret model terraces as shortening structures formed by thrust-fault-related folding (Fig. 6). Under this interpretation, the surface strain on a cone that down-flexes its basement (Fig. 6a) is accommodated by shear fractures that penetrate some distance into the cone and that may be surface-breaking (Fig. 6b: 1). Terraces on the cone's flanks develop as hanging wall anticlines above these thrusts (Fig. 6b: 2). That folding contributes to terrace morphology is supported by the identification (with PIV) of areas in extension inside the leading edge of well-developed terraces in some models. This deformation is consistent with localized outer-arc extension of the terrace hanging wall anticline as the structure continues to accumulate strain, since it is observed on those terraces that are amongst the longest active structures.

The arrangement of terraces in a fishscale pattern (Byrne *et al.* 2009) is probably due to a constrictional strain regime in the central region of the down-sagged volcano-basement system. As shown by PIV (Fig. 3), the horizontal displacements of the sagging cone are directed inwards towards its summit. This displacement field must lead to a combination of both radial and concentric components of shortening in the horizontal plane (see Holohan *et al.* 2013), with a corresponding component of vertical lengthening lying normal to this plane (Fig. 7). Horizontal displacement (heave) along the fishscale arrangement of terrace-bounding thrust faults resolves both the radial and concentric shortening components, whereas the vertical displacement (throw) on the faults and related folds accommodates the associated lengthening along the vertical axis.

The dip angle of the terrace-bounding faults in our models remains an open question, however, because the viscous response of the silicone putty used in our experiments precluded the cross-sectioning of the models. Continued sagging during sectioning of a wetted model would have yielded unrealistic strains. Under a scenario where maximum and intermediate principal stresses lie in the horizontal plane (i.e.  $\sigma_3$  is vertical), terrace faults probably dip into the cone at angles of approximately 30° (e.g. Fig. 6b: 1). Should these principal stresses be slope-parallel (i.e.  $\sigma_3$  normal to the cone surface: van Wyk de Vries & Matela 1998), however, and where cone slope is relatively high (>20°), the terrace-bounding faults may be near-horizontal or even inclined down-slope.

Another key question concerns the timing of terrace formation on Mars. Little evidence remains

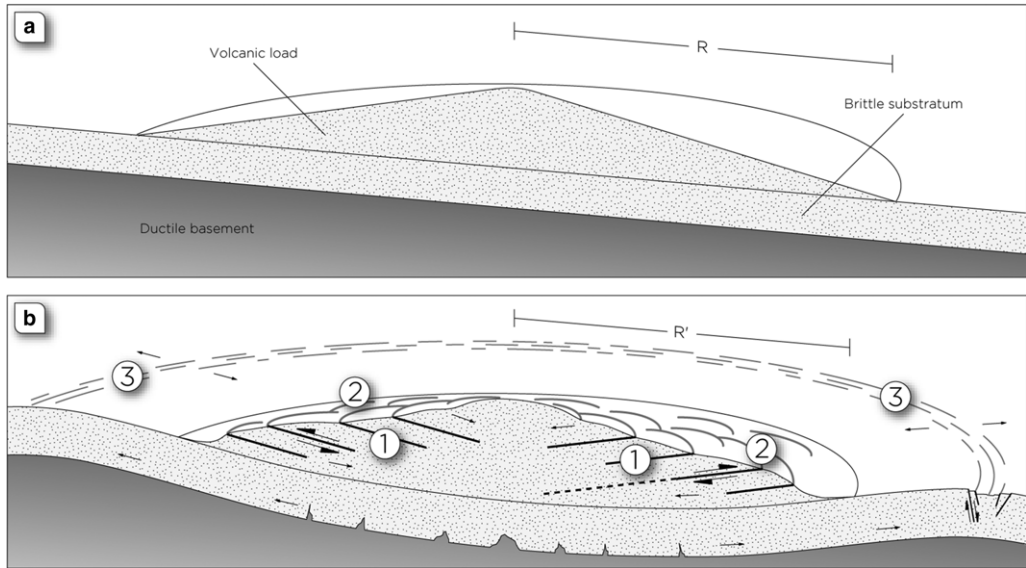


**Fig. 6.** Schematic block diagrams of a conical volcano atop a brittle substratum, both of which are underlain by a ductile basement, (a) before and (b) after the onset of sagging. This behaviour results in (1) the development of blind or surface-breaking thrust faults that penetrate some distance into the cone's interior. These thrusts may dip down into the cone (as shown here) or, depending on its slope and the exact orientations of the principal stresses, they may be near-horizontal or even outwards-dipping. (2) Hanging-wall anticlines form above these thrusts and describe a fishscale map pattern on the volcano's flanks. (3) Deformation of the cone is accompanied by the growth of an extensional annulus concentric to the load. In (b), small arrows indicate movement directions; half-arrow pairs indicate the assumed sense of slip on faults.  $R$  is the initial cone radius;  $R'$  is the final cone radius. Adapted from Byrne *et al.* (2013).

regarding the onset or cessation of flank terracing on Martian volcanoes (Byrne *et al.* 2009). The convexities visible within 1 min of cone emplacement in volcano-loading models (Fig. 3a) may be lobate slumps formed during the construction of the cone (cf. Cecchi *et al.* 2005) that were later (i.e. after *c.* 5 min) reactivated as terrace-bounding faults during sagging. If so, then asperities upon a volcano could influence the subsequent locations of flank-shortening structures. If these faint structures are terraces, however, then remarkably low strains are required for their formation. Terraces may thus rapidly form early in the flexural process, serving to further localize flank shortening amid continued volcano sagging during or after the active lifetime of the edifice.

The time taken for structures to develop in these experiments, about 10 min, is equivalent to approximately 68 000 years using our time scaling ratio,  $T^*$ , for ductile material. This is an extremely short time for deformation to occur with respect to the accepted ages of Martian volcanoes (e.g. Plescia & Saunders 1979; Werner 2009; Platz & Michael 2011; Platz *et al.* 2011) and is reliant on the viscosity parameter chosen for the ductile Martian lithosphere. If the choice of viscosity value is correct, then we might infer that flank terraces

form rapidly on volcanoes that were largely complete by the time lithospheric flexure began. However, if our value is too low, then the lithosphere's flexural response may post-date volcanic construction considerably. A viscosity value that is too high implies that flexure, and hence terracing, may have occurred during the main shield-building phase. Since the possible viscosity range for Mars' ductile lithosphere is extremely wide, our temporal scaling factor is not well constrained. Nevertheless, the flank shortening represented by terraces is of the order of only a few per cent (Byrne *et al.* 2009), and so it is likely that neither substantial nor long-lived volcano sagging is required to form the terraces we observe today.

Although terracing may be initially distributed along most of the cone's flanks (and presumably its interior), PIV analysis shows that strain accumulation on the terraces (and, in some cases, the formation of new terraces) becomes increasingly concentrated on the lowermost slopes as sagging progresses. This latter finding is broadly consistent with the results of McGovern & Solomon (1993), who used finite-element numerical models to predict failure within, and proximal to, an edifice down-flexing an elastic plate that overlaid a viscoelastic mantle. In their models of a load emplaced

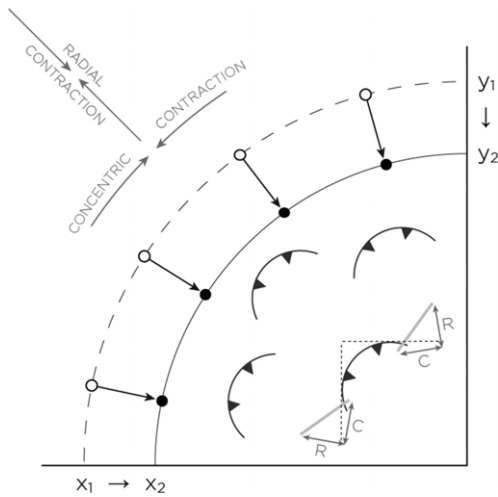


**Fig. 7.** Schematic sketch of how the fishscale pattern of flank terraces may arise through a combination of horizontal contractions orientated radially and concentrically to the centre of a conical load. Circumferential horizontal shortening, in addition to radial shortening, results as material points on the cone move radially inwards towards the cone summit (note the reduction of the arc length from  $x_1$  to  $x_2$  and from  $y_1$  to  $y_2$ ). The fishscale arrangement of the terrace-bounding faults enables across-fault contraction (solid light grey lines) to resolve both the radial and concentric components of shortening (dark grey lines, labelled ‘R’ and ‘C’, respectively). Modified from Holohan *et al.* (2013).

instantaneously upon a 40 km-thick elastic lithosphere, these authors found a similar down-slope propagation of circumferentially orientated thrust faulting as the underlying lithosphere flexes (see McGovern & Solomon 1993, fig. 8b–d). McGovern & Solomon (1993) inferred that initial faulting is restricted to high flank elevations before shifting down-slope, such that most of the upper edifice surface is in failure. In contrast, we observe more widely distributed terracing at first, with on-going deformation increasingly localized at lower-flank elevations. One reason for this discrepancy could be that model terracing on upper-mid slopes develops so quickly that we are unable to observe its propagation at the temporal resolution of the time-lapse images.

The models of McGovern & Solomon (1993) also predicted normal faulting initially at the base of the cone, which then migrates outwards on the surrounding surface. The outwards movement of extension about the edifice in these authors’ models is also similar to the broadening of the load-concentric extensional annulus (Fig. 6b: 3) that we observe in our models as sagging continues. This

behaviour indicates that as the cone down-flexes its basement, the diameter of the flexural bowl is reduced, presumably as it deepens, in a manner consistent with the change in flexural profile associated with numerical models of viscoelastic deformation of Earth’s oceanic lithosphere (e.g. Watts & Zhong 2000, fig. 12).

### *The effects of variations in experimental parameters*

The strength and effective elastic thickness of the lithosphere are closely linked to its seismogenic (i.e. brittle) thickness (Watts & Burov 2003). In particular, effective flexural rigidity scales with brittle thickness to the third power (see the supplementary material of Byrne *et al.* 2013), and so even small changes in its brittle thickness may have large effects on the basement’s flexural response to loading. This is manifest in our models, where decreasing the basal brittle-layer thickness ( $B$ ) progressively reduced its capacity to support its superposed load. For a given cone volume (e.g. 1325 cm<sup>3</sup>), sand–plaster layers with  $B < 30$  mm led to the formation of deeper flexural depressions, as well as narrower annular extensional zones and flexural rises that developed closer to the load, than for models where  $B = 30$  mm. Cones atop thinner brittle layers, therefore, experienced commensurately more sagging, and distributed strain into more (albeit smaller) structures, than cones on thicker layers. The change in flexural profile with successively thinner sand–plaster layers increasingly constricted a greater portion of the cone, which probably accounts for why terraces formed at progressively greater flank elevations as  $B$  tended to zero. Conversely, and consistent with the findings of Byrne *et al.* (2013) (see below), a sufficiently large value of  $B$  with respect to cone height would inhibit flexure, and hence terrace formation, altogether.

The emplacement of a cone with angle-of-repose slopes but with smaller volumes than the standard experimental set-up produced proportionately fewer, smaller terraces, but otherwise terrace formation was little affected. That the number and size of terraces that formed on these models was consistently lower presumably reflects the correspondingly smaller surface areas of the lower-volume cones. This finding suggests that the model structures are scale-invariant, as has been concluded for Martian flank terraces (Byrne *et al.* 2009). Changes to flank slope angle reduced the expression of terraces. Surface contraction was nevertheless observed across all cones during sagging, even when terraces were not visible. The reduced expression or absence of terraces on lower-angle

cones may, in part, be an experimental limitation, with the sand–plaster mix partly accommodating the much lower contractional surface strains in these models volumetrically (i.e. via grain flow) only.

Whilst cone height did not scale to natural values in most experiments, comparable deformation behaviour was observed in models with low cone slopes (e.g.  $10\text{--}20^\circ$ ), as in those with slopes at the angle of repose of the granular material used (e.g. Fig 5b). The shallower depressions in the silicone, and less overall surface displacement, in lower-slope models relative to angle-of-repose cones were probably the result of their lower weight and volume. In addition, the ratios of cone height to brittle basement thickness in our experiments fall within the range of values in which volcano-induced flexure is likely to occur on Earth, according to the dimensionless parameter  $\Pi_{\text{sag}}$  developed by Byrne *et al.* (2013). This parameter relates a volcano's loading of its basement (as a function of its weight and volume) to the resistance of the basement to flexure (i.e. its flexural rigidity) (see the supplementary material of Byrne *et al.* 2013 for more detail). The  $\Pi_{\text{sag}}$  values for all experiments in this study (including those of differing volume and cone slope) extend from  $9.5 \times 10^{-3}$  to  $1.39 \times 10^2$ , well within the range of about  $1 \times 10^{-5}$ – $1.1 \times 10^3$  for Terrestrial volcanoes (Byrne *et al.* 2013). Although they are not known, similar values for Mars as for Earth are assumed for the purposes of this study.

Cones with eccentric planforms displayed more prominent terracing along flank sectors parallel, and less prominent terracing along sectors perpendicular, to the major axis. Such a pattern of terracing is probably a function of the same subsidence at the cone centre being accommodated over a greater horizontal distance along sectors perpendicular to the major axis than on parallel sectors. Consequently, flanks perpendicular to the cone's long axis undergo lower strains (cf. Holohan *et al.* 2008), and so less prominent terracing, than flanks lying parallel to the long axis.

Our results therefore indicate that terraces may form across a range of cone geometries, independent of cone volume, flank slope, planform and probably all but the greatest brittle basement thicknesses. On the basis of gross structural similarities between volcanoes with low slopes in nature, numerical studies with low edifice slopes (e.g. McGovern & Solomon 1993; Borgia 1994; van Wyk de Vries & Matela 1998) and the analogue model results shown here, we are confident that the main structural relationships observed in our experiments are geologically realistic representations of real-world, volcano-induced lithospheric flexure. We explore this inference in the next section.

## Comparison of model results with natural examples

### *Flank terraces*

The flank structures formed in these flexural experiments share the convex-upwards, outwards-verging morphology and imbricate ‘fishscale’ plan-view stacking pattern of volcano flank terraces on Mars (compare Figs 1 & 3). Therefore, on the basis of their strong similarity to our model results, we consider Martian volcano flank terraces to be hanging-wall anticlines over blind or surface-breaking thrust faults that formed in a constrictional regime applied to a volcano as it flexed downwards. If this interpretation is correct, then flank terraces are a kinematic volcano equivalent to lobate scarps, landforms occurring widely on Mercury, Mars and the Moon that are thought to form above thrust faults that accommodate crustal shortening (Strom *et al.* 1975; Nahm & Schultz 2011; Watters *et al.* 2012).

Moreover, the systematic formation of laboratory terraces on cones of varying slopes and volumes is consistent with observations of Martian volcanoes. Both large (e.g. Olympus Mons) and small (e.g. Hecates Tholus) shields are terraced (Fig. 1a, d), as are volcanoes with different slopes – for example, Elysium Mons and Alba Patera (*c.*  $7^\circ$  and  $1^\circ$ , respectively) (Plescia 2004). Even in low-slope models where terraces were not observed, these cones still displayed the same general style of surface deformation as cones at the angle of repose.

Further, that fewer, larger terraces form in models that feature intermediate to thick (i.e.  $B = 15\text{--}30$  mm) brittle basal-layer thicknesses (Figs 3b & 4a) matches observations at volcanoes for which photogeological and gravity/topography admittance studies have returned the highest estimates of  $T_e$  (Thurber & Toksöz 1978; Comer *et al.* 1985; Zuber *et al.* 2000; McGovern *et al.* 2004; Belleguic *et al.* 2005; Beuthe *et al.* 2012). Whilst estimates for lithosphere thicknesses differ between studies, in all cases the relative differences between high and low  $T_e$  values are the same. Specifically, Ascraeus and Olympus Montes are consistently quoted as being supported by the thickest lithosphere of all Martian volcanoes, and these volcanoes display the most prominent and longest terraces (Byrne *et al.* 2009) (Fig. 1). This observation is consistent with our model results. Although the range of  $\Pi_{\text{sag}}$  values for which lithospheric flexure will occur on Mars remains to be determined, a key test will be to determine whether terraces occur on Mars' smaller shields, and to relate the gravitational load of such volcanoes to the rigidity of their supporting basement.

We note that model terraces lack the snub-nosed roundness characteristic of most observed terraces

(Byrne *et al.* 2009), and feature a generally flattened upper surface instead. However, photogeological data indicate that terraces on Mars have been covered, and their forms tempered, by contemporaneous or subsequent erupted material (Thomas *et al.* 1990). The analogue structures may thus correspond to the terrace form prior to being mantled by erupted material. Moreover, whereas our models generally produced terraces arranged

axisymmetrically about a cone, terraces on Martian volcanoes are often less evenly distributed (e.g. Hecates Tholus, Fig. 1d). Aeolian or mass-wasting processes – coupled with differences in edifice geometry, internal architecture, regional slopes and near- and far-field stresses – probably contribute to the observed asymmetry in terrace distributions on Martian shields (Byrne *et al.* 2009, 2013).

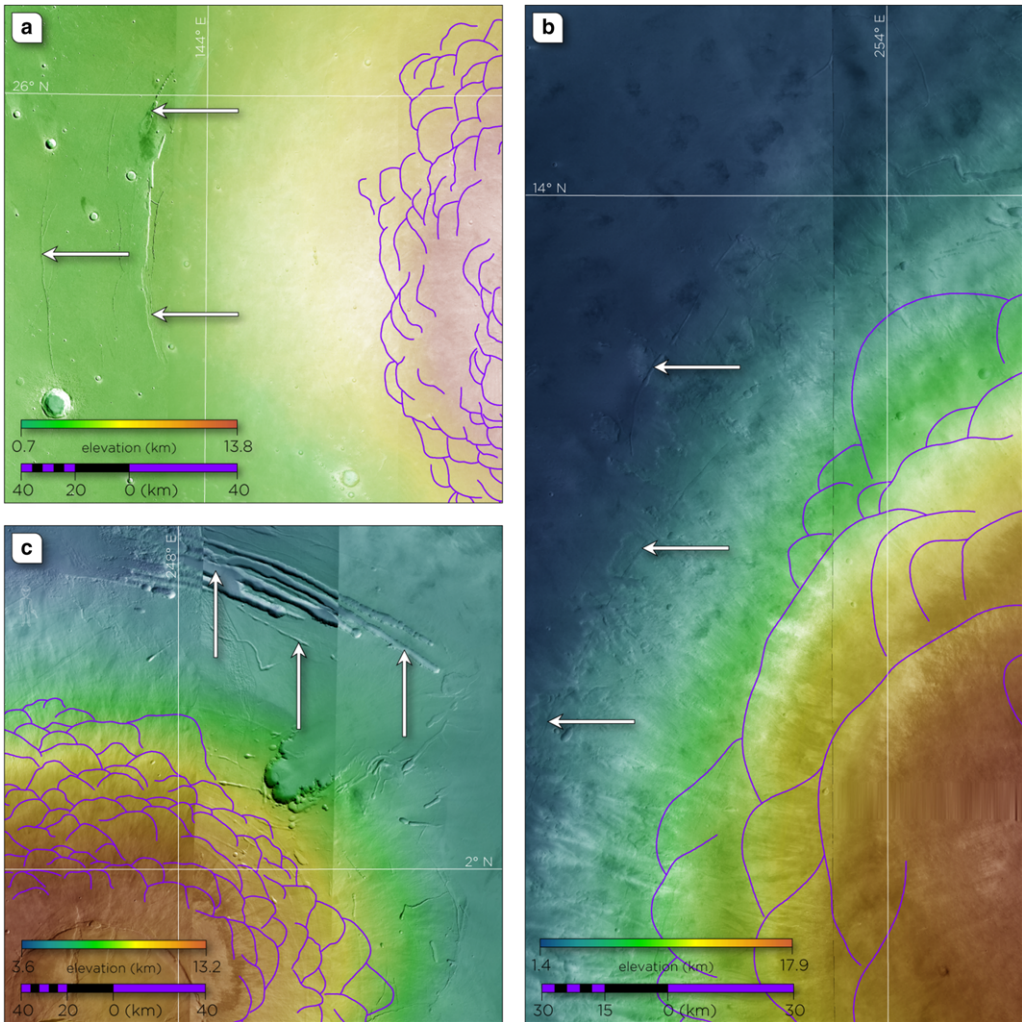


**Fig. 8.** Examples of volcano-concentric graben (marked by white arrows) centred on or spatially associated with terraced Martian volcanoes (a) Elysium, (b) Ascraeus and (c) Pavonis Montes. The images are portions of High Resolution Stereo Camera (HRSC) images (Neukum *et al.* 2004) from the ESA Mars Express spacecraft: (a) h1295\_0000, h1317\_0000 and h7424\_0000; (b) h1217\_0001 and h1206\_0001; and (c) h0891\_0000, h2175\_0000 and h3276\_0000 – shown with colour-coded MOLA elevation data and with terrace outlines (purple) from Byrne *et al.* (2009). Each image is shown in an azimuthal equidistant projection, centred at (a) 24.5°N, 145°E, (b) 12°N, 253.7°E and (c) 2°N, 248°E.

Finally, there is precedent for associating extension with the development of shortening structures, as is observed for some terraces (e.g. Fig. 3d). For example, lobate scarps can exhibit extensional faults along the crests of their forelimbs (Mueller & Golombek 2004; Morley 2007; Watters & Johnson 2010). Extension along model terraces may therefore be manifest in nature as faults and/or fissures, which in places might have influenced the locations of later pit crater chains (interpreted to have formed due to dilational faulting: Ferrill *et al.* 2004; Wyrick *et al.* 2004) on, for example, the mid and upper flanks of Ascraeus Mons (Byrne *et al.* 2012).

### *Flexural trough*

One of the distinguishing features of lithospheric loading is the formation of a flexural trough or moat concentric to the load (e.g. McGovern & Solomon 1997). Given their large masses, Martian volcanoes can be expected to display measurable vertical deflections of the lithosphere (Comer *et al.* 1985; Zuber *et al.* 1993). Such troughs are not readily visible on photogeological images, but can be identified with geophysical data. On the basis of topographical profiles or gravitational field models, flexural troughs have been identified or inferred for several large crustal loads on Mars, including Olympus Mons (Zuber & Smith 1997), the Tharsis Rise (Solomon & Head 1982) and the planet's entire southern hemisphere (Watters 2003).

The difficulty in resolving these features directly may, in part, be due to infilling by material such as landslide deposits (McGovern & Solomon 1997) and lavas from smaller, nearby shields or from fissures (e.g. Bleacher *et al.* 2007). Evidence for the latter process in particular is given by the embayed margins of several Tharsis and Elysium volcanoes by younger lavas (e.g. Plescia 2004). A very low amplitude relative to wavelength (Zuber *et al.* 1993) will also render a flexural trough difficult to detect. In any case, assuming these depressions do form part of the flexural response of the Martian lithosphere to volcano loading, they correspond to the concentric troughs observed in our experiments.

### *Annular graben*

If bending stresses associated with lithospheric flexure due to a major volcanic load are sufficiently high, extensional fractures will form concentric to and outside of the load (Comer *et al.* 1985; Williams & Zuber 1995). Load-concentric fractures have been observed on Earth (Lambeck & Nakiboglu 1980), associated with mascons on the Moon (Melosh 1978; Solomon & Head 1980) and related

to large crustal loads on Mars, including its volcanoes (Comer *et al.* 1985).

It is likely, therefore, that extensional structures such as the ring fractures about Elysium Mons (Plescia 2004) (Fig. 8a), the arcuate graben that cross-cut the western flank of Ascraeus Mons (Byrne *et al.* 2012) (Fig. 8b) and the group of prominent troughs at the NE base of Pavonis Mons (Crumpler & Aubele 1978) (Fig. 8c) correspond to load-concentric fractures formed in the laboratory. In the models, extension is spatially associated with the flexural bulge encircling the load, and so it is reasonable to assume that this structural arrangement also applies to the Martian examples.

We note that models of volcano-induced flexure as configured in this study cannot account for the 6–8 km-high basal scarp that encircles Olympus Mons (e.g. Carr *et al.* 1977). However, Byrne *et al.* (2013) showed that the addition of a silicone layer beneath the edifice acts to decouple it from its underlying basement, so that although flexure-induced constriction of a cone is accommodated on its mid to upper flanks by distributed terracing, as before, outwards-directed slip (i.e. volcano spreading) of the cone is enabled along the silicone layer (see Byrne *et al.* 2013, fig. 3b). Flexural slip along such a basal décollement produces a large monoclinical fold around the cone's base, the leading edge of which can oversteepen and collapse. This structural outcome strongly resembles the overall morphology of Olympus Mons (see their Fig. 4b), indicating that the solar system's largest volcano formed through the hybrid action of volcano sagging and spreading.

## **Summary and concluding remarks**

In experiments where a brittle conical load at the angle of repose was emplaced upon a dual-layer (brittle and ductile) basement, the near-surface regions of the load entered a constrictional strain regime as the cone–basement system down-sagged or 'flexed'. The region under the cone developed into a bowl-shaped depression that, in conjunction with the opposite-facing lowermost flank of the cone, formed a load-concentric flexural trough. Beyond the trough an annular zone of extension developed, whereas the cone's mid and lower flanks experienced a net reduction of surface area. Associated horizontal radial and concentric shortening was accommodated by the formation of convex, outwards-verging terrace structures arranged in an axisymmetrical fishscale pattern about the cone.

The expression of flank terraces, in terms of number, size and distribution, was strongly influenced by the thickness of the brittle upper-basement layer (our analogue to the seismogenic lithosphere).

With a sufficiently great brittle-layer thickness, basement flexure and terrace formation was inhibited entirely. However, reducing the thickness of the brittle upper layer, ultimately to zero, promoted greater sagging, with the flexural wavelength of the basement decreasing whilst its amplitude increased. Progressively thinner brittle layers resulted in the formation of smaller terraces at greater flank elevations until, with the upper layer absent, the zone of terracing extended almost to the cone summit. In comparison, variations in cone volume, slope or eccentricity had only minor effects on the development of flank terracing.

Our experimental results bear strong similarities in morphology and spatial distribution to flank terraces on Mars, to systems of arcuate graben attributed to volcano-induced flexure of the Martian lithosphere and to geophysical signatures interpreted to be buried or in-filled flexural troughs surrounding several of the largest shield volcanoes on that planet. These similarities provide compelling support for the conclusion that Martian flank terraces are flexurally induced structures, formed to accommodate surface shortening of a shield volcano as it down-flexes its basement. The horizontal contraction of an edifice during flexure may inhibit the ascent of magma to summit elevations (McGovern 2007; Byrne *et al.* 2012), whilst serving to enhance the overall structural integrity of the volcano (Byrne *et al.* 2013). A full understanding of the structural evolution of large shield volcanoes on Mars therefore requires that they be appraised within the context of lithospheric flexure.

We thank M. Bonini, T. Platz and M. Massironi for helpful reviews that improved this manuscript. P. K. Byrne and V. R. Troll thank the Enterprise Ireland International Collaboration Programme (grant No. IC/2006/37/ED-209) and the TekNat faculty at Uppsala University for support during several stages of this research. E. P. Holohan acknowledges a Marie Curie International Mobility Fellowship co-funded by Marie Curie Actions and the Irish Research Council. M. Kervyn acknowledges the support of a Research Credit from the Fonds voor Wetenschappelijke Onderzoek (FWO) for developing the analogue modelling laboratory at VUB. This research has made use of NASA's Planetary Data System and Astrophysics Data System.

## References

BELLEGUIC, V., LOGNONNÉ, P. & WIECZOREK, M. 2005. Constraints on the Martian lithosphere from gravity and topography data. *Journal of Geophysical Research*, **110**, E11005, <http://dx.doi.org/10.1029/2005JE002437>

BEUTHE, M., LE MAISTRE, S., ROSENBLATT, P., PÄTZOLD, M. & DEHANT, V. 2012. Density and lithospheric thickness of the Tharsis Province from MEX MaRS

and MRO gravity data. *Journal of Geophysical Research*, **117**, E04002, <http://dx.doi.org/10.1029/2011JE003976>

BLEACHER, J., GREELEY, R., WILLIAMS, D., CAVE, S. & NEUKUM, G. 2007. Trends in effusive style at the Tharsis Montes, Mars, and implications for the development of the Tharsis Province. *Journal of Geophysical Research*, **112**, E09005, <http://dx.doi.org/10.1029/2006JE002873>

BORGIA, A. 1994. Dynamic basis of volcanic spreading. *Journal of Geophysical Research*, **99**, 17 791–17 804.

BORGIA, A., DELANEY, P. & DENLINGER, R. 2000. Spreading volcanoes. *Annual Review of Earth and Planetary Sciences*, **28**, 539–570.

BYRNE, P. K., VAN WYK DE VRIES, B., MURRAY, J. B. & TROLL, V. R. 2009. The geometry of volcano flank terraces on Mars. *Earth and Planetary Science Letters*, **281**, 1–13.

BYRNE, P. K., VAN WYK DE VRIES, B., MURRAY, J. B. & TROLL, V. R. 2012. A volcanotectonic survey of Ascraeus Mons, Mars. *Journal of Geophysical Research*, **117**, E01004, <http://dx.doi.org/10.1029/2011JE003825>

BYRNE, P. K., HOLOHAN, E. P., KERVYN, M., VAN WYK DE VRIES, B., TROLL, V. R. & MURRAY, J. B. 2013. A sagging-spreading continuum of large volcano structure. *Geology*, **41**, 339–342.

CARR, M. H., GREELEY, R., BLASIUS, K. R., GUEST, J. E. & MURRAY, J. B. 1977. Some Martian volcanic features as viewed from the Viking orbiters. *Journal of Geophysical Research*, **82**, 3985–4015.

CECCHI, E., VAN WYK DE VRIES, B. & LAVEST, J.-M. 2005. Flank spreading and collapse of weak-cored volcanoes. *Bulletin of Volcanology*, **67**, 72–91.

COMER, R. P., SOLOMON, S. C. & HEAD, J. W. 1985. Mars: thickness of the lithosphere from the tectonic response to volcanic loads. *Reviews of Geophysics*, **23**, 61–92.

CRUMPLER, L. S. & AUBELE, J. C. 1978. Structural evolution of Arsia Mons, Pavonis Mons and Ascraeus Mons: Tharsis region of Mars. *Icarus*, **34**, 496–511.

CRUMPLER, L. S., HEAD, J. W. & AUBELE, J. C. 1996. Calderas on Mars: characteristics, structure and associated flank deformation. In: MCGUIRE, W. J., JONES, A. P. & NEUBERG, J. (eds) *Volcano Instability on the Earth and Other Planets* Geological Society, London, Special Publications, **110**, 307–348.

DELCAMP, A., VAN WYK DE VRIES, B. & JAMES, M. R. 2008. The influence of edifice slope and substrata on volcano spreading. *Journal of Volcanology and Geothermal Research*, **177**, 925–943.

DONNADIEU, F. & MERLE, O. 1998. Experiments on the indentation process during cryptodome intrusions: new insights into Mount St. Helens deformation. *Geology*, **26**, 79–82.

FERRILL, D. A., WYRICK, D. Y., MORRIS, A. P., SIMS, D. W. & FRANKLIN, N. M. 2004. Dilational fault slip and pit chain formation on Mars. *GSA Today*, **14**, 4–12.

HODGES, C. & MOORE, H. 1994. *Atlas of Volcanic Landforms on Mars* United States Geological Survey, Professional Papers, **1534**.

HOLOHAN, E. P., TROLL, V. R., VAN WYK DE VRIES, B., WALSH, J. J. & WALTER, T. R. 2008. Unzipping Long

- Valley: an explanation for vent migration patterns during an elliptical ring fracture explosion. *Geology*, **36**, 323–326.
- HOLOHAN, E. P., WALTER, T. R., SCHÖPFER, M. P. J., WALSH, J. J., VAN WYK DE VRIES, B. & TROLL, V. R. 2013. Origins of oblique-slip faulting during caldera subsidence. *Journal of Geophysical Research: Solid Earth*, **118**, 1778–1794.
- HUBBERT, M. K. 1951. Mechanical basis for certain familiar geologic structures. *Geological Society of America Bulletin*, **62**, 355–372.
- ISHERWOOD, R. J., JOZWIAK, L. M., JANSEN, J. C. & ANDREWS-HANNA, J. C. 2013. The volcanic history of Olympus Mons from paleo-topography and flexural modeling. *Earth and Planetary Science Letters*, **363**, 88–96.
- KERVYN, M., BOONE, M. N., VAN WYK DE VRIES, B., LEBAS, E., CNUDE, V., FONTIJN, K. & JACOBS, P. 2010. 3D imaging of volcano gravitational deformation by computerized X-ray micro-tomography. *Geosphere*, **6**, 482–498.
- LAMBECK, K. & NAKIBOGLU, S. M. 1980. Seamount loading and stress in the ocean lithosphere. *Journal of Geophysical Research*, **85**, 6403–6418.
- LOHRMANN, J., KUKOWSKI, N., ADAM, J. & ONCKEN, O. 2003. The impact of analogue material properties on the geometry, kinematics, and dynamics of convergent sand wedges. *Journal of Structural Geology*, **25**, 1691–1711.
- MCGOVERN, P. J. 2007. Flexural stresses beneath Hawaii: implications for the October 15, 2006, earthquakes and magma ascent. *Geophysical Research Letters*, **34**, L23305, <http://dx.doi.org/10.1029/2007GL031305>
- MCGOVERN, P. J. & MORGAN, J. K. 2009. Volcanic spreading and lateral variations in the structure of Olympus Mons, Mars. *Geology*, **37**, 139–142.
- MCGOVERN, P. J. & SOLOMON, S. C. 1993. State of stress, faulting, and eruption characteristics of large volcanoes on Mars. *Journal of Geophysical Research*, **98**, 23 553–23 579.
- MCGOVERN, P. J. & SOLOMON, S. C. 1997. Some implications of a basal detachment structural model for Olympus Mons. In: *Proceedings of the 28th Annual Lunar and Planetary Science Conference, March 17–21, 1997, Abstract Volume* LPI Contribution **1090**. Lunar and Planetary Institute, Houston, TX, 913.
- MCGOVERN, P. J., SOLOMON, S. C. *ET AL.* 2004. Correction to: localized gravity/topography admittance and correlation spectra on Mars: Implications for regional and global evolution. *Journal of Geophysical Research*, **109**, E07007, <http://dx.doi.org/10.1029/2004JE002286>
- MC SWEENEY, H. Y., JR, GROVE, T. L. & WYATT, M. B. 2003. Constraints on the composition and petrogenesis of the Martian crust. *Journal of Geophysical Research*, **108**, 5137, <http://dx.doi.org/10.1029/2003JE002175>
- MELOSH, H. J. 1978. The tectonics of mascon loading. In: *Proceedings of the 9th Lunar and Planetary Science Conference, Houston, Texas, March 13–17, 1978, Volume 3*. LPI Contribution **1575**. Pergamon Press, New York, 3513–3525.
- MERLE, O. & BORGIA, A. 1996. Scaled experiments of volcanic spreading. *Journal of Geophysical Research*, **101**, 13 805–13 817.
- MORGAN, J. & MCGOVERN, P. 2005. Discrete element simulations of gravitational volcanic deformation: 1. deformation structures and geometries. *Journal of Geophysical Research*, **110**, B05402, <http://dx.doi.org/10.1029/2004JB003252>
- MORLEY, C. K. 2007. Variations in late Cenozoic–Recent strike-slip and oblique-extensional geometries, within Indochina: the influence of pre-existing fabrics. *Journal of Structural Geology*, **29**, 36–58.
- MORRIS, E. 1981. Structure of Olympus Mons and its basal scarp. In: *Abstracts of Papers Presented to the Third International Colloquium on Mars, held in Pasadena, California, August 31–September 2, 1981* LPI Contribution **441**. Lunar and Planetary Institute, Houston, TX, 161.
- MOUGINIS-MARK, P., WILSON, L., HEAD, J., BROWN, S., HALL, J. & SULLIVAN, K. 1984. Elysium Planitia, Mars: regional geology, volcanology, and evidence for volcano-ground ice interactions. *Earth, Moon, and Planets*, **30**, 149–173.
- MUELLER, K. & GOLOMBEK, M. 2004. Compressional structures on Mars. *Annual Review of Earth and Planetary Sciences*, **32**, 435–464.
- NAHM, A. L. & SCHULTZ, R. A. 2011. Magnitude of global contraction on Mars from analysis of surface faults: implications for Martian thermal history. *Icarus*, **211**, 389–400.
- NEUKUM, G., JAUMANN, R. *ET AL.* 2004. *HRSC – The High Resolution Stereo Camera of Mars Express* European Space Agency, Special Publications, **ESA SP-1240**.
- OEHLE, J.-F., VAN WYK DE VRIES, B. & LABAZUY, P. 2005. Landslides and spreading of oceanic hot-spot and arc shield volcanoes on Low Strength Layers (LSLs): an analogue modeling approach. *Journal of Volcanology and Geothermal Research*, **144**, 169–189.
- PLATZ, T. & MICHAEL, G. 2011. Eruption history of the Elysium Volcanic Province, Mars. *Earth and Planetary Science Letters*, **312**, 140–151.
- PLATZ, T., MÜNN, S., WALTER, T. R., PROCTER, J. N., MCGUIRE, P. C., DUMKE, A. & NEUKUM, G. 2011. Vertical and lateral collapse of Tharsis Tholus, Mars. *Earth and Planetary Science Letters*, **305**, 445–455.
- PLESCIA, J. B. 2000. Geology of the Uranian Group Volcanic Constructs: Uranus Patera, Ceraunius Tholus, and Uranus Tholus. *Icarus*, **143**, 376–396.
- PLESCIA, J. B. 2004. Morphometric properties of Martian volcanoes. *Journal of Geophysical Research*, **109**, E03003, <http://dx.doi.org/10.1029/2002JE002031>
- PLESCIA, J. B. & SAUNDERS, R. 1979. The chronology of the Martian volcanoes. In: *Proceedings of the 10th Lunar and Planetary Science Conference, Houston, Texas, March 19–23, 1979, Volume 3*. LPI Contribution **1576**. Pergamon Press, New York, 2841–2859.
- RAMBERG, H. 1981. *Gravity, Deformation and the Earth's Crust*, 2nd edn. Academic Press, London.
- SHELLART, W. P. 2000. Shear test results for cohesion and friction coefficients for different granular materials: scaling implications for their usage in analogue modelling. *Tectonophysics*, **324**, 1–16.
- SMITH, D. E., ZUBER, M. T. *ET AL.* 2001. Mars orbiter laser altimeter: experiment summary after the first year of

- global mapping of Mars. *Journal of Geophysical Research*, **106**, 23,689–23,722.
- SOLOMON, S. C. & HEAD, J. W. 1980. Lunar mascon basins: lava filling, tectonics, and evolution of the lithosphere. *Reviews of Geophysics and Space Physics*, **18**, 107–141.
- SOLOMON, S. C. & HEAD, J. W. 1982. Evolution of the Tharsis province, Mars: the importance of heterogeneous lithospheric thicknesses on volcanic construction. *Journal of Geophysical Research*, **87**, 9755–9774.
- STROM, R. G., TRASK, J. J. & GUEST, J. E. 1975. Tectonism and volcanism on Mercury. *Journal of Geophysical Research*, **80**, 2478–2507.
- TEN GROTENHUIS, S. M., PIAZOLO, S., PAKULA, T., PASSCHIER, C. W. & BONIS, P. D. 2002. Are polymers suitable rock analogs? *Tectonophysics*, **350**, 35–47.
- THOMAS, P. J., SQUYRES, S. W. & CARR, M. H. 1990. Flank tectonics of Martian volcanoes. *Journal of Geophysical Research*, **95**, 14 345–14 355.
- THURBER, C. H. & TOKSÖZ, M. N. 1978. Martian lithospheric thickness from elastic flexure theory. *Geophysical Research Letters*, **5**, 977–980.
- VAN WYK DE VRIES, B. & MATELA, R. 1998. Styles of volcano-induced deformation: numerical models of substratum flexure, spreading and extrusion. *Journal of Volcanology and Geothermal Research*, **81**, 1–18.
- WALTER, T. R. 2011. Structural architecture of the 1980 Mount St. Helens collapse: an analysis of the Rosenquist photo sequence using digital image correlation. *Geology*, **39**, 767–770.
- WALTER, T. & TROLL, V. R. 2001. Formation of caldera periphery faults: an experimental study. *Bulletin of Volcanology*, **63**, 191–203.
- WATTERS, T. R. 2003. Lithospheric flexure and the origin of the dichotomy boundary on Mars. *Geology*, **31**, 271–274.
- WATTERS, T. R. & JOHNSON, C. L. 2010. Lunar tectonics. In: WATTERS, T. R. & SCHULTZ, R. A. (eds) *Planetary Tectonics* Cambridge University Press, Cambridge, 121–182.
- WATTERS, T. R., ROBINSON, M. S., BANKS, M. E., THANH, T. & DENEVI, B. W. 2012. Recent extensional tectonics on the Moon revealed by the Lunar Reconnaissance Orbiter Camera. *Nature Geoscience*, **5**, 181–185.
- WATTS, A. B. & BUROV, E. B. 2003. Lithospheric strength and its relationship to the elastic and seismogenic layer thickness. *Earth and Planetary Science Letters*, **213**, 113–131.
- WATTS, A. B. & ZHONG, S. 2000. Observations of flexure and the rheology of oceanic lithosphere. *Geophysical Journal International*, **142**, 855–875.
- WEIJERMARS, R., JACKSON, M. P. A. & VENDEVILLE, B. 1993. Rheological and tectonic modeling of salt provinces. *Tectonophysics*, **217**, 143–174.
- WERNER, S. C. 2009. The global Martian volcanic evolutionary history. *Icarus*, **201**, 44–68.
- WILLIAMS, K. K. & ZUBER, M. T. 1995. An experimental study of incremental surface loading of an elastic plate: application to volcano tectonics. *Geophysical Research Letters*, **22**, 1981–1984.
- WYRICK, D., FERRILL, D. A., MORRIS, A. P., COLTON, S. L. & SIMS, D. W. 2004. Distribution, morphology, and origins of Martian pit crater chains. *Journal of Geophysical Research*, **109**, E06005, <http://dx.doi.org/10.1029/2004JE002240>
- ZIMBLEMAN, J. & EDGETT, K. 1992. The Tharsis Montes, Mars: comparison of volcanic and modified landforms. In: *Proceedings of the 22nd Lunar and Planetary Science Conference, Houston, Texas, March 18–22, 1991* LPI Contribution **1588**. Lunar and Planetary Institute, Houston, TX, 31–44.
- ZUBER, M. T. & SMITH, D. E. 1997. Mars without Tharsis. *Journal of Geophysical Research: Planets*, **10**(E12), 28 673–28 685.
- ZUBER, M. T., BILLS, B. G., FREY, H. V., KIEFER, W. S., NEREM, R. S. & ROARK, J. H. 1993. Possible flexural signatures around Olympus and Ascræus Montes, Mars. In: *Proceedings of the 24th Lunar and Planetary Science Conference, March 15–19, 1993, Houston, Texas* LPI Contribution **1590**. Lunar and Planetary Institute, Houston, TX, 1591–1592.
- ZUBER, M. T., SOLOMON, S. C. *ET AL.* 2000. Internal structure and early thermal evolution of Mars from Mars Global Surveyor topography and gravity. *Science*, **287**, 1788–1793.
- ZUCCA, J., HILL, D. & KOVACH, R. 1982. Crustal structure of Mauna Loa volcano, Hawaii, from seismic refraction and gravity data. *Bulletin of the Seismological Society of America*, **72**, 1535–1550.